Mechanism of Electrochemical Proton Reduction Catalyzed by a Cobalt Tetraaza Schiff Base Macrocyclic Complex: Ligand Protonation and/or Influence of Chloro Ligand?

Margaux Willery, Paul-Gabriel Julliard, Florian Molton, Fabrice Thomas, Jérôme Fortage, Cyrille Costentin, Marie-Noëlle Collomb

Mechanism of Electrochemical Proton Reduction Catalyzed by a Cobalt Tetraaza Schiff Base Macrocyclic Complex: Ligand Protonation and/or Influence of Chloro Ligand?

Margaux Willery, Paul-Gabriel Julliard, Florian Molton, Fabrice Thomas, Jérôme Fortage,* Cyrille Costentin* and Marie-Noëlle Collomb*

Univ Grenoble Alpes, DCM, CNRS, 38000 Grenoble, France.

Keywords: Hydrogen Evolution, Electrochemistry, Catalysis, Cobalt tetraaza complexes, Mechanism

ABSTRACT: Cobalt complexes with tetra- and penta-aza macrocyclic ligands including the pyridyldiimine motif isolated by Busch as early as the 1970s is a very promising family of catalysts that were only quite recently exploitated for both electro- and photo-catalytic HER and CO_2RR. In particular, the tetra-aza $[Co^{III}(CR14)Cl_2]^+$ (CR14 = 2,12-dimethyl-3,7,11,17-tetraazabicyclo[11.3.1]heptadeca-1(17),2,11,13,15-pentaene) appears to be one of the most efficient and stable Co catalyst in pure aqueous solution for HER. In this work we reinvestigated the H_2-evolving mechanism catalyzed by this complex in organic solvent (CH_3CN) with the acid *p*-cyanoanilinium tetrafluoroborate as a proton source. By comparison of $[Co^{III}(CR14)Cl_2]^+$ and $[Co^{III}(CR14)(CH_3CN)_2]^{3+}$ electrochemical behavior with and without addition of chloride we first characterized the thermodynamical coordination and decoordination properties of the chloro ligands at the Co^{III}, Co^{II} and Co^{I} formal redox states. Then, we showed (through echem, UV-Visible absorption and EPR) that addition of *p*-cyanoanilinium facilitates chloro ligand decoordination at the Co^{II} state rather than protonation of a nitrogen of the ligand. The mechanism of *p*-cyanoanilinium acid electroreduction catalyzed by $[Co^{III}(CR14)(CH_3CN)_2]^{3+}$ is then characterized kinetically by a thorough cyclic voltammetry analysis. The resting state in the bulk solution in the course of constant potential electrolysis for *p*-cyanoanilinium acid reduction was identified as a non-protonated $[Co^{II}(CR14)(CH_3CN)_x]^{2+}$ (x = 1 or 2) species whereas it is proposed that a Co^{II} hydride is the resting state in the diffusion-reaction layer.

Introduction

Intense research over the last fifteen years has been devoted to the development of efficient molecular catalysts for the electro- and photo-induced reduction of protons into dihydrogen (Hydrogen Evolution Reaction, HER) and the reduction of CO_2 (CO_2 reduction reaction (CO_2RR)).[1-2] Molecular catalysts present the advantages of having tunable redox properties and, for CO_2RR, good selectivity.[3-4] The most widely employed families of catalysts for HER based on non-precious metals are cobaloximes, complexes of cobalt with polypyridine ligands, nickel with pyridine/thiolate or phosphine ligands (Dubois' catalyst) and diiron carbonyl hydrogenases mimics.[3-12] For CO_2RR, they mainly rely on iron, cobalt and nickel complexes with macrocyclic ligands (porphyrin, phthalocyanine, corrole, cyclam) and manganese with bipyridine/carbonyl ligands.[13-14] Cobalt complexes with tetra- and penta-aza macrocyclic ligands including the pyridyl-diimine motif (Scheme 1), isolated as early as the 1970s,[15] are also a very promising family of catalysts quite recently exploitated for both electro- and photo-induced HER[16-31] and CO_2RR,[32-40] in homogeneous and heterogeneous conditions.[28-29, 41-43] In particular, the tetra-azamacrocyclic Schiff base complex $[Co^{III}(CR14)(X)_2]^{n+}$ (CR14 = 2,12-dimethyl-3,7,11,17-tetraazabicyclo[11.3.1]heptadeca-1(17),2,11,13,15-pentaene, X = Cl (n = 1) or H_2O (n = 3) has received an increase of interest in the recent years as it is now considered as one of the most efficient and stable H_2-evolving molecular catalyst in fully aqueous solution.[16-21, 23-27, 44-45] The outstanding performances of this complex have been initially attributed to the stability of its doubly reduced state generated during the catalysis, formally denoted "Co^{I}" (a low-spin Co^{II} antiferromagnetically coupled to a ligand based anion radical is also a possible configuration) promoted by the macrocyclic nature of the ligand.[18-19, 33] This stability prevents degradation of the complex in reducing conditions. Moreover, we have shown that, in CH_3CN, the electrogenerated "Co^{I}" state is easily protonated by the relatively strong *p*-cyanoanilinium acid (pK_a = 7.0) leading to the spontaneous generation of half an equivalent of H_2 along with the quantitative reoxidation of the complex into its Co^{II} form, *via* the formation of an elusive Co^{III} hydride intermediate (denoted Co^{III}–H) (Scheme 2a, equation (1)).[21]

$$"Co^{I}" + n\,H^+ \rightarrow "Co^{III}H" \rightarrow "Co^{II}" + \frac{1}{2}H_2 + (n-1)H^+ \qquad (1)$$

Based on these experimental results and on computational studies, it can be proposed that the most probable reaction pathway for H_2 formation is the reduction of Co^{III}-H by Co^{I} to produced Co^{II}-H that is further protonated (heterolytic mechanism via Co^{II}-H), *i.e.* an ECEC mechanism alternating a one-electron reduction and a protonation step. DFT calculations indeed indicate that the calculated standard potential of the Co^{III}–H/Co^{II}–H couple is more positive than the standard potential of the Co^{II}/Co^{I} couple.[25]

Scheme 1. Structures of the mentioned tetra- and penta-aza macrocylic complexes and of the *p*-cyanoanilinium tetrafluoroborate.

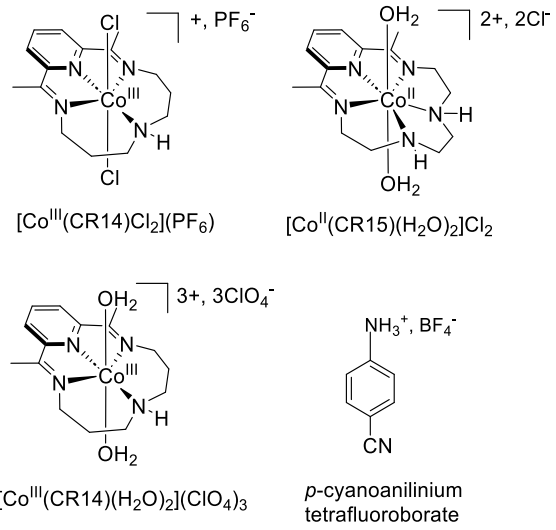

$[Co^{III}(CR14)Cl_2](PF_6)$ $[Co^{II}(CR15)(H_2O)_2]Cl_2$

$[Co^{III}(CR14)(H_2O)_2](ClO_4)_3$ *p*-cyanoanilinium tetrafluoroborate

To explain the quite exceptional performance of this complex for HER, the involvement of the secondary amine of the macrocycle ligand as an intramolecular proton relay for dihydrogen formation has been proposed.[27, 30] Experimentally, the electrocatalytic reduction of *p*-cyanoanilinium acid in CH_3CN was proposed to undergo a fast protonation of the amine of the ligand upon reduction from the Co^{III} to the Co^{II} state together with the decoordination of this amine (Scheme 2b).[27] This suggestion is based on changes observed in EPR spectroscopy upon addition of acid on the "Co^{II}" state which signal changes from a broad to a better resolved signal with superhyperfine structure and in cyclic voltammetry with a significant shift to more positive potential of the Co^{III}/Co^{II} wave, that partly loses reversibility. An ECEC mechanism was also proposed for H_2 evolution (equations (3)-(6)) except that the species entering the catalytic cycle is the protonated "$Co^{II}LH$" species (equation (2)) and that this protonated amine can act as an intramolecular proton relay during H_2 production (equation (6)).

$$Co^{III}L + H^+ + e^- \rightarrow "Co^{II}LH" \quad (2)$$

$$"Co^{II}LH" + e^- \rightarrow "Co^{I}LH" \quad (3)$$

$$"Co^{I}LH" + H^+ \rightarrow "Co^{III}HLH" \quad (4)$$

$$"Co^{III}HLH" + e^- \rightarrow "Co^{II}HLH" \quad (5)$$

$$"Co^{II}HLH" + H^+ \rightarrow Co^{II}LH" + H_2 \quad (6)$$

An intramolecular dihydrogen formation for this complex and the analogous methyl derivative between a Co^{II}–H and an ammonium proton of the macrocyclic amine ligand was also evoked under photochemical conditions.[25, 30] However, according to DFT calculations, this pathway was considered not likely because of the high energy barrier required for the previous steps involving amine protonation and decoordination and the significant rearrangement of the molecule with regards to the intermolecular pathway (interaction of Co^{II}–H and one proton of a water molecule). Interestingly, the decoordination of one of the amine of the ligand was also pointed out in the case of the hepta-coordinated penta-aza-macrocyclic cobalt complex $[Co^{II}(CR15)(H_2O)_2]Cl_2$ (CR15 = 2,13-dimethyl-3,6,9,12,18-pentaazabicyclo[12.3.1]octadeca-1(18),2,12,14,16-pentaene) in CH_3CN, which comprises a larger macrocycle with five nitrogen atoms.[21] In that case, the decoordination occurs upon reduction of the Co^{II} to the low-valent "Co^{I}" form and without added acid (Scheme 2c). While this pendant amine could act as a proton relay promoting H_2 formation *via* proton-coupled electron transfer (PCET) reactions, it increases the flexibility of the macrocycle making the catalyst less robust in the Co^{I} state.

Scheme 2. (a) Mechanism of HER by the addition of *p*-cyanoanilinium on a CH_3CN solution of electrogenerated $[Co^{I}(CR14)(CH_3CN)]^+$ complex leading to the spontaneous formation of ½ H_2 and Co^{II} complex (adapted from reference [18]), (b) proposed protonation/decoordination of the amine of the ligand upon reduction of Co^{III} into Co^{II} in CH_3CN in the presence of 5 eq. of *p*-cyanoanilinium acid (adapted from reference [27]) and (c) proposed change in geometry of $[Co^{II}(CR15)(CH_3CN)_2]^{2+}$ induced by reduction into Co^{I} in CH_3CN (adapted from reference [21]).

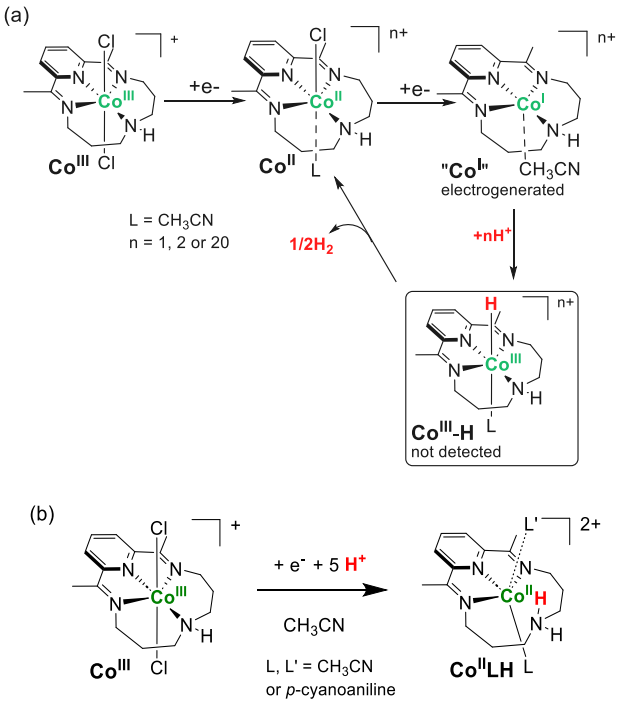

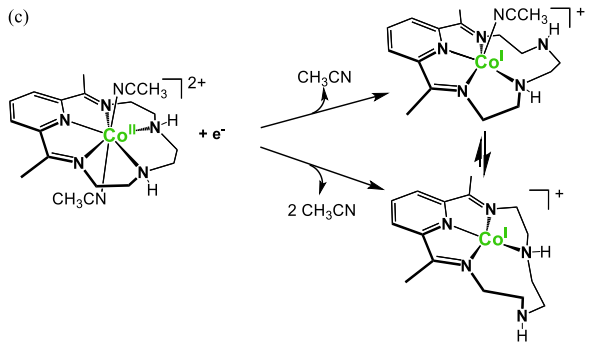

The above-mentioned studies show that the cobalt centre formally swings between Co^{III}, Co^{II} and Co^{I} redox states during catalysis with variable ligand environments. Recent investigations have shed light on the peculiar role of ligand coordination/decoordination in molecular catalysis of electrochemical reactions.[46] In particular, it is crucial to get and regenerate an open coordination site for catalysis to occur. In that regard, starting with $[Co^{III}(CR14)Cl_2](PF_6)$ complex, it seems important to take into consideration in the reaction mechanism and in kinetics characterization the possible role of chloro ligands and investigate whether or not some experimental features attributed to nitrogen ligands could result from chloro ligand coordination/decoordination. In the present work, we have thus first investigated in detail the redox behavior and spectroscopic properties of $[Co^{III}(CR14)(H_2O)_2](ClO_4)_3$ and $[Co^{III}(CR14)Cl_2](PF_6)$ complexes with and without exogeneous chloride ions by cyclic voltammetry, by electrolysis coupled to UV-Visible absorption and EPR spectroscopy. Note that the aquo ligands of $[Co^{III}(CR14)(H_2O)_2]^{3+}$ are readily displaced by CH_3CN molecule upon dissolution in this solvent as previously evidenced by UV-Visible absorption spectroscopy.[18, 21] We will therefore refer to this complex as the acetonitrile complex "$[Co^{III}(CR14)(CH_3CN)_2]^{3+}$" in the course of the manuscript or simply as "$[Co^{III}(CR14)]^{3+}$". Similarly, at other formal oxidation states, namely Co^{II}, Co^{I} or Co^{0}, acetonitrile ligands are not indicated unless stated otherwise, in particular when discussing EPR data (vide infra). These studies allow a thorough thermodynamic characterization of chloro ligands coordination/decoordination at the various redox states. With this information in hand, we have reinvestigated the H_2-evolving mechanism in organic solvent (CH_3CN) in presence of *p*-cyanoanilinium tetrafluoroborate with particular emphasis on the behavior of mono-reduced form of $[Co^{III}(CR14)(CH_3CN)_2]^{3+}$ as a catalyst. We have also identified the resting state in the bulk solution in the course of electrocatalysis so as to probe the possible involvement of a nitrogen of the ligand as proton relay for the tetra-aza cobalt complex at the Co^{II} state.

Results and Discussion

Thermodynamic characterization of chloro ligands coordination/decoordination.

The study of the redox behavior of $[Co^{III}(CR14)Cl_2]^+$ by cyclic voltammetry in CH_3CN is complicated by the presence of the two chloro ligands in axial positions that undergo decoordination/substitution by solvent molecules upon reduction to the Co^{II} and Co^{I} states and recoordination upon reoxidation to Co^{III}, as shown in a previous work.[18] In order to study the effect of the chloride on the coordination sphere of the one- and two-electrons reduced states of this complex, the electrochemical and spectroscopic properties of $[Co^{III}(CR14)(CH_3CN)_2]^{3+}$ and of its electrogenerated one and two-electron reduced forms were investigated in the presence of increasing amount of chloride ions (Cl^-) and analyzed in the framework of the square scheme mechanism depicted in Scheme 3. All thermodynamic constants (association equilibrium constants in M^{-1} and standard potentials in V vs. Ag^+/Ag; all potentials are given vs. this reference electrode throughout the paper) are defined in Scheme 3. Previous X-ray structural characterization[33] of the mono- and doubly reduced forms of the acetonitrile complex reveals five-coordinate $[Co^{II}(CR14)(CH_3CN)]^{2+}$ and $[Co^{I}(CR14)(CH_3CN)]^{+}$ species with a distorted square-planar pyramid geometry. However, in CH_3CN solution, the number of CH_3CN may vary and, as seen below. For Co^{II}, an equilibrium between the penta- and hexacoordinated species $[Co^{II}(CR14)(CH_3CN)]^{2+}$ and $[Co^{II}(CR14)(CH_3CN)_2]^{2+}$ has been evidenced by EPR spectroscopy, while for the Co^{I}, the tetra- and pentacoordinated species, $[Co^{I}(CR14)]^{+}$ and $[Co^{I}(CR14)(CH_3CN)]^{+}$, are possible configurations in solution according to our previous calculations.[19, 47] We will thus refer to these complexes as $[Co^{II}(CR14)(CH_3CN)_x]^{2+}$ (x = 1 or 2) and $[Co^{I}(CR14)(CH_3CN)_x]^{+}$ (x = 0 or 1) in the course of the manuscript or, for the sake of simplicity, as $[Co^{II}(CR14)]^{2+}$ and $[Co^{I}(CR14)]^{+}$. As shown in Figure 1a, an electrogenerated solution of $[Co^{II}(CR14)]^{2+}$ (see the Supporting Information (SI) for details) exhibits two successive one electron reversible reduction waves and one quasi-reversible oxidation wave. The standard potentials of the corresponding formal Co^{III}/Co^{II}, Co^{II}/Co^{I} and Co^{I}/Co^{0} redox couples are respectively at $E^0_{III/II}$ = 0.29, $E^0_{II/I}$ = -0.79 and $E^0_{I/0}$ = -1.79 V vs. Ag^+/Ag. If the oxidation wave is clearly a metal-centered process, Co^{III}/Co^{II}, the two reduction waves can be either metal or ligand centered, *i.e.* on one of the imine of the macrocycle, as previously described.[18-19, 33]

Scheme 3. Chloro ligand coordination/decoordination. Acetonitrile ligand are not shown.

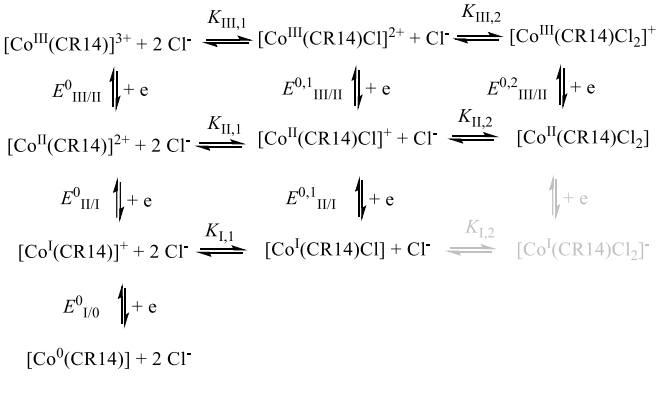

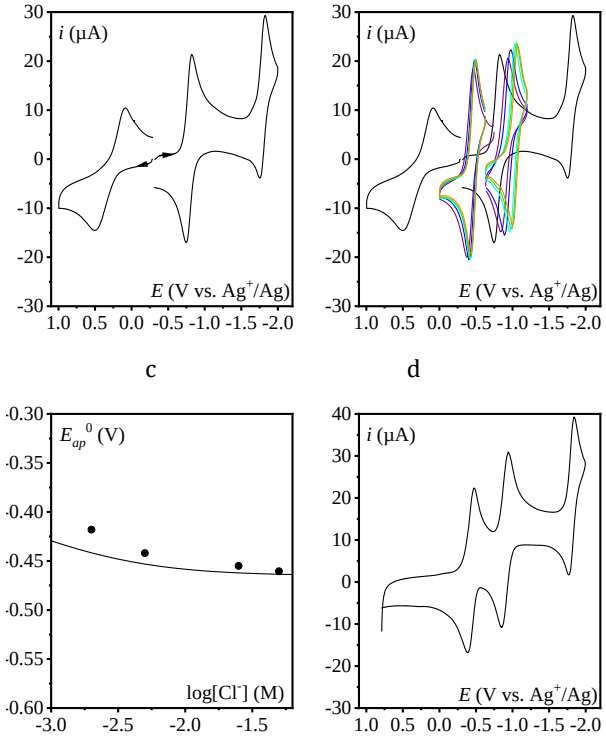

Figure 1. CVs at a 3 mm diameter glassy carbon electrode of (a) a 1 mM solution of $[Co^{II}(CR14)(CH_3CN)_x]^{2+}$ (x = 1 or 2) in CH_3CN, 0.1 M $[Bu_4N]ClO_4$ at 0.1 V/s and (b) after addition of increasing amounts of Et_4NCl: 2 (violet), 5 (blue), 25 (light blue), 50 (light green), 100 (orange) mM. (c) Apparent standard potential of the Co^{III}/Co^{II} couple as function of added chloride; the full line corresponds to equation 10 (see text). (d) CV at a 3 mm diameter glassy carbon electrode of a 1 mM solution of $[Co^{III}(CR14)Cl_2]^+$ in CH_3CN, 0.1 M $[Bu_4N]ClO_4$ at 0.1 V/s.

Upon addition of chloride ions (from 2 to 100 mM), the Co^{III}/Co^{II} wave is shifted cathodically (Figure 1b) reaching a limit value that can be estimated to be the standard potential of the $[Co^{III}(CR14)Cl_2]^+/[Co^{II}(CR14)Cl_2]$ couple, $E^{0,2}_{III/II}$ = -0.465 V (Figure 1c). The Co^{III}/Co^{II} wave is thus substantially shifted by about 750 mV due to the higher electrostatic effect of the chloro ligands compared to CH_3CN ligands which stabilization effect is much stronger on Co^{III} than on Co^{II}.

Starting from $[Co^{III}(CR14)Cl_2]^+$ (1 mM) in the absence of free chloride ion, a one electron reversible wave is observed at an apparent standard potential $E^{0,ap}_{III/II}$ located at -0.43 V (Figure 1d). Because its value is different from $E^{0,2}_{III/II}$, we can infer that it corresponds to the $[Co^{III}(CR14)Cl_2]^+/[Co^{II}(CR14)Cl]^+ + Cl^-$ couple, the reduction of Co^{III} into Co^{II} inducing the release of one chloro ligand that can be substituted by one CH_3CN molecule. [17-18] Its fast recoordination at the Co^{III} state makes the Co^{III}/Co^{II} system quite reversible. Therefore, we have $E^{0,ap}_{III/II} \approx E^{0,2}_{III/II} + \frac{RT}{F}\ln\left(1+1/\frac{1}{K_{II,2}\left[Cl^-\right]}\right)$. Hence, taking $\left[Cl^-\right]$ equal to 1 mM, we obtain $K_{II,2}$ = 342 M^{-1}. Similarly, a second reversible wave is observed at an apparent standard $E^{0,ap}_{II/I}$ located at -0.88 V (Figure 1d). If we consider that decoordination of the chloro ligand is fast at the Co^{I} state, then this apparent standard potential corresponds to the $[Co^{II}(CR14)Cl]^+/[Co^{I}(CR14)]^+ + Cl^-$ couple; hence taking $\left[Cl^-\right]$ = 1 mM and $E^{0}_{III/II} \approx E^{0,ap}_{II/I} + \frac{RT}{F}\ln\left(1+K_{II,1}\left[Cl^-\right]\right)$; we obtain $K_{II,1}$ = 32530 M^{-1}. Knowing $K_{II,2}$ and $K_{II,1}$, we can calculate the speciation of Co^{II} at any total Cl^- concentration for a total concentration of complexes equal to 1 mM (Figure 2a). It is for example seen that at a 2 mM total Cl concentration, *i.e.* starting with $[Co^{III}(CR14)Cl_2]^+$ and quantitatively converting it to "Co^{II}", a mixture of *ca*. 80% $[Co^{II}(CR14)Cl]^+$ and 20% $[Co^{II}(CR14)Cl_2]$ is obtained with negligible amount of $[Co^{II}(CR14)]^{2+}$. These equilibrium constants and the resulting speciation are confirmed by UV-Vis spectra obtained from $[Co^{II}(CR14)]^{2+}$ in the presence of various amount of added chloride ions (Figure 2b). $[Co^{II}(CR14)]^{2+}$ UV-Vis spectrum has a sharp band at 357 nm and a large band at 446 nm with shoulders at 470, 548 and 639 nm (black line in Figure 2b). In the presence of large excess of chloride (100 mM), the UV-Vis spectrum of $[Co^{II}(CR14)Cl_2]$ is observed (orange line in Figure 2b) with bands at 415 nm, a shoulder at 456 and 498 nm and additional bands at 533, 636 and 729 nm. The UV-Vis absorption spectrum of $[Co^{II}(CR14)Cl]^+$ (violet line in Figure 2b) is obtained by taking into account that quantitative electrolysis of $[Co^{III}(CR14)Cl_2]^+$ gives a mixture of 76% $[Co^{II}(CR14)Cl]^+$ and 21% $[Co^{II}(CR14)Cl_2]$ and 3% $[Co^{II}(CR14)]^{2+}$. It thus appears that the Co^{II}-mono-chloro complex has a weak band at 393 nm and a large one at 499 nm. From these three spectra, the experimental spectra obtained by addition of 5 mM and 25 mM of chloride ions on a 1 mM solution of $[Co^{II}(CR14)]^{2+}$ were simulated taking into account the expected speciation of "Co^{II}" complexes calculated in Figure 2a. As shown in Figure 2b (blue and green lines), the simulated spectra overlay with the experimental spectra thus indicating that the evaluated speciation is correct and confirming the equilibrium constants values extracted from electrochemical data.

a b

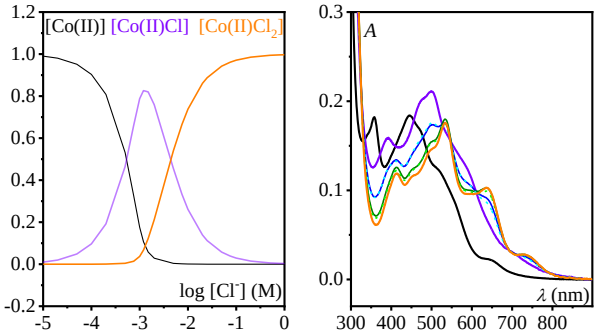

Figure 2. (a) Speciation of "Co^{II}" species (total cobalt complexes concentration at 1 mM) as function of total chloride concentration. (b) UV-Visible absorption spectra changes of a 1 mM solution of $[Co^{II}(CR14)(CH_3CN)_x]^{2+}$(x = 1 or 2) in CH_3CN 0.1 M $[Bu_4N]ClO_4$ (l = 1 mm), initial solution (black) and after addition of 100 mM of Et_4NCl: formation of $[Co^{II}(CR14)Cl_2]$ (orange); extraction of the UV-Vis spectrum of $[Co^{II}(CR14)Cl]^+$ (violet, see text); UV-Vis spectra after respectively addition of 5 mM and 25 mM of chloride ions on a 1 mM solution of $[Co^{II}(CR14)(CH_3CN)_x]^{2+}$ (blue and green, dashed spectra are calculated spectra taken into account speciation of Co^{II} for 5 mM and 25 mM of added chloride ions, see text).

X-band EPR spectroscopy can also bring relevant information on the coordination sphere of the paramagnetic Co^{II} species. EPR signals typical of a low-spin d^7 Co^{II} centre were obtained at 100 K, but the spectra exhibit distinct features depending on the presence or not of chloro ligands (Figure 3). In the absence of Et_4NCl (Figure 3a, purple spectrum) the spectrum of an electrogenerated solution of $[Co^{II}(CR14)]^{2+}$ is slightly rhombic as reflected by the g-values g_x = 2.283, g_y = 2.163, g_z = 2.016. It exhibits well-defined lines in the g_z components, which are due to the hyperfine coupling with the ^{59}Co center (I_{Co} = 7/2, A_z = 262 MHz). A super-hyperfine pattern could be additionally observed, demonstrating the coupling with ^{14}N nucleus (A_z = 41 MHz) from N-donor ligand(s) in axial position.[48-50] This spectrum is in close correspondence with the one reported in reference [27] after electrochemical or chemical one-electron reduction of $[Co^{III}(CR14)Cl_2]^+$ in CH_3CN solvent in presence of 5 equiv. of *p*-cyanoanilinium tetrafloroborate (see below). Each resonance is splitted into 3 main lines, completed by two outer lines. However, integration of the most resolved super-hyperfine splitted resonances shows that the intensity ratio is neither 1:1:1 for the three main lines (as expected for the coupling with a single ^{14}N nucleus), nor 1:2:3:2:1 for the five lines (as expected for the coupling with two ^{14}N nucleus) (Figure 3b and S8). Thus, the signal rather corresponds to the superposition of two distinct signals (3- and 5-lines patterns), which is confirmed by acid titration (vide infra)).[50] This is consistent with the presence of an equilibrium between penta- and hexa-coordinated species $[Co^{II}(CR14)(CH_3CN)]^{2+}$ and $[Co^{II}(CR14)(CH_3CN)_2]^{2+}$, in agreement with previous DFT calculations.[21] To further support the hypothesis that the superhyperfine structure is due to exogeneous nitrogen ligand(s) (specifically, the coordination of CH_3CN ligand(s) in axial position), we note the absence of such structure in the EPR spectra of the structurally characterized $[Co^{II}(CR14)(CH_3CN)]^{2+}$ dissolved in a mixture of THF/DMF[33] solvents or of $[Co^{II}(CR14)(H_2O)_2]^{2+}$ (Figure 3a).[18] Both spectra indeed show only the hyperfine structure. In the presence of 2-5 mM of Et_4NCl (Figure 3a, blue and light blue spectra), the EPR spectrum obtained is broad due to the coordination of at least one chloro ligand (see below), and was simulated by considering an axial signal and using the parameters g_x = g_y = 2.20, g_z = 2.01, A_z = 270 MHz. Note that the addition of larger amounts of Et_4NCl improves the resolution of the spectrum, resulting in the appearance of a multi-line pattern in the central resonances of the g_z component. The resonance spacing (55 MHz) suggests an interaction with multiple nitrogens. Unfortunately, it was not possible to extract further information due to significant overlaps and a large uncertainty in the determination of A_z for the cobalt centre.

a

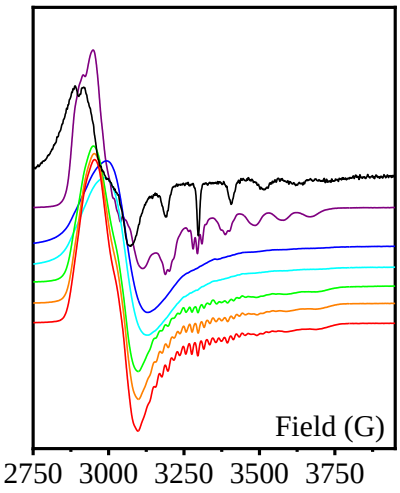

b

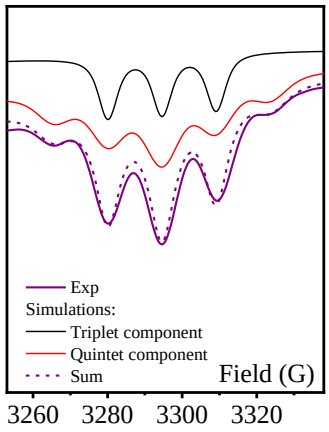

Figure 3. (a) 100 K EPR spectra of a 1 mM electrogenerated solution of $[Co^{II}(CR14)(CH_3CN)_x]^{2+}$ (x = 1 or 2) (purple) in CH_3CN, 0.1 M $[Bu_4N]ClO_4$ and after addition of increasing amount of Et_4NCl (from 2 (blue), 5 (light blue), 25 (light green), 50 (orange) and 100 (red). EPR parameters: (blue) g_x = g_y = 2.20, g_z = 2.01, A_z = 270 MHz, g-strain = 0.05 (purple) g_x = 2.283, g_y = 2.163, g_z = 2.015, A_z = 262 MHz

(Co), 41 MHz (N).)); and (black) comparison with the 100 K EPR spectrum of $[Co^{II}(CR14)(H_2O)_2]^{2+}$ (x = 1 or 2) (0.5 mM) in H_2O (EPR parameters: g_x = 2.305, g_y = 2.221, g_z = 2.015, $A_x = A_y$ = 0 G, A_z = 302 MHz) from reference[18] (A in MHz is obtained by multiplying the value in G by 1.39×g). (b) Zoom showing the simulation of the resonance centered at 3295 G (most resolved one) of the sample in the absence of Et_4NCl. Microwave Freq. 9.42 GHz, power 7 mW, Mod. Freq. 100 KHz, Amp. 5 G. Full range simulations are given in SI.

The reduction wave corresponding to the Co^{II}/Co^{I} state in the presence of various amount of added chloride ions (Figure 1b) can be described via the lower double square scheme of Scheme 3. Consequently, assuming fast kinetics for all steps and considering that the formation of $[Co^{I}(CR14)Cl_2]^-$ is unlikely, the reversible CV position is characterized by an apparent standard potential $E^{0,ap}_{II/I}$, with:

$$E^{0,ap}_{II/I} = E^{0}_{II/I} + \frac{RT}{F}\ln\left(\frac{1+K_{I,1}\left[Cl^-\right]}{1+K_{II,1}\left[Cl^-\right]+K_{II,1}K_{II,2}\left[Cl^-\right]^2}\right) \quad (7)$$

Knowing $K_{II,2}$ and $E^{0}_{II/I}$, $K_{I,1}$ = 65 M^{-1} is obtained from the adjustment of experimental data with equation 7 (Figure 4a). Then, $E^{0,1}_{II/I}$ = -0.952 V is obtained from the thermodynamical relationship:

$$E^{0,1}_{II/I} = E^{0}_{II/I} + \frac{RT}{F}\ln\left(\frac{K_{I,1}}{K_{II,1}}\right). \quad (8)$$

The value of $K_{I,1}$ is further confirmed from the speciation of $[Co^{I}(CR14)]^+$ and $[Co^{I}(CR14)Cl]$ obtained from UV-Vis spectra recorded at various added amount of chloride ions on an electrogenerated 1 mM solution of $[Co^{I}(CR14)]^+$ (see SI for details) (Figures 4b and 4c).

a

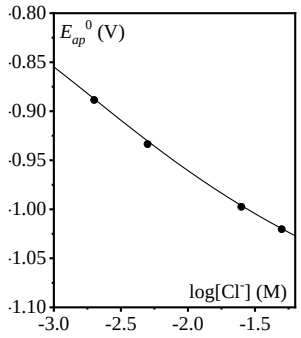

b c

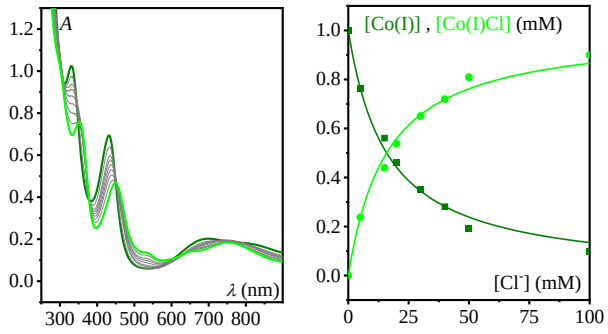

Figure 4. (a) Apparent standard potential of the Co^{II}/Co^{I} couple of 1 mM solution of $[Co^{II}(CR14)(CH_3CN)_x]^{2+}$ as function of the concentration of added chloride ion. Line: fitting using equation 7 (see text). (b) UV-Visible absorption spectra changes of a 1 mM solution of $[Co^{I}(CR14)]^+$ in CH_3CN 0.1 M $[Bu_4N]ClO_4$, initial solution (dark green) and after addition of increasing amount of Et_4NCl (grey) up to 100 mM (light green) (l = 1 mm). (c) Speciation of $[Co^{I}(CR14)]^+$ (dark green) and $[Co^{I}(CR14)Cl]$ (light green) as function of added Et_4NCl concentration. Line: fitting (see SI for details).

The chloride coordination equilibrium constants at the Co^{III} redox state are expected to be large. Hence, as soon as a small amount of chloride is added to $[Co^{III}(CR14)]^{3+}$, $[Co^{III}(CR14)Cl]^{2+}$ and $[Co^{III}(CR14)Cl_2]^+$ are formed quantitatively. According to thermodynamic relationships, we have:

$$E^{0,2}_{III/II} = E^{0}_{III/II} + \frac{RT}{F}\ln\left(\frac{K_{II,1}K_{II,2}}{K_{III,1}K_{III,2}}\right) \quad (9)$$

Therefore, knowing $E^{0}_{III/II}$, $E^{0,2}_{III/II}$, $K_{II,2}$ and $K_{II,1}$, we obtain $K_{III,1} \times K_{III,2}$ = 7 10^{19} M^{-2}. Additional data are required to get individual values of $K_{III,1}$ and $K_{III,2}$. When 0 to 2 mM of chloride is added to a 1 mM solution of $[Co^{III}(CR14)]^{3+}$, the CVs show a transition from a reversible wave corresponding to the $[Co^{III}(CR14)]^{3+}/[Co^{II}(CR14)]^{2+}$ redox couple to the $[Co^{III}(CR14)Cl_2]^+/[Co^{II}(CR14)Cl]^+ + Cl^-$ redox couple (Figure 5). Interestingly, when less than two equivalents of chloride ions per Co center are added, a small wave is observed at intermediate potentials, *ca.* -0.07 V. This wave is tentatively attributed to the reduction of $[Co^{III}(CR14)Cl]^{2+}$. A very crude estimation of the equilibrium constant $K_{III,1}$ is thus 10^{12} M^{-1} which would lead to $E^{0,1}_{III/II}$ in the range of -0.15 V and $K_{III,2}$ around 7 10^{7} M^{-1}.

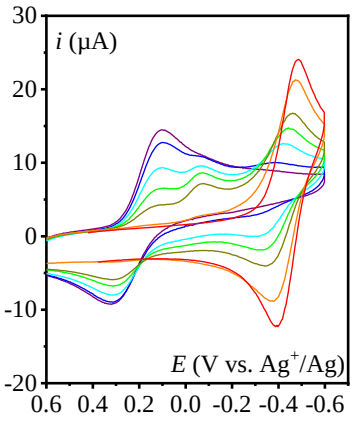

Figure 5. CVs at a 3 mm diameter glassy carbon electrode of a 1 mM solution of $[Co^{III}(CR14)(CH_3CN)_2]^{3+}$ (violet) in CH_3CN, 0.1 M $[Bu_4N]ClO_4$ at 0.1 V/s and after addition of increasing amounts of Et_4NCl: 0.1 (blue), 0.5 (light blue), 0.75 (light green), 1 (dark yellow), 1.5 (orange), 2 (red) mM.

Table 1. Thermodynamic constants

Standard potential (V vs. Ag^+/Ag)			
	$j=0$	$j=1$	$j=2$
$E^{0,j}_{III/II}$	0.29	-0.15	-0.465
$E^{0,j}_{II/I}$	-0.79	-0.95	-
$E^{0,j}_{I/0}$	-1.79	-	-
Equilibrium constant (M^{-1})			
	$i = III$	$i = II$	$i = I$
$K_{i,1}$	10^{12}	$3.25\ 10^4$	65
$K_{i,2}$	$7\ 10^7$	$3.4\ 10^2$	-

A full thermodynamic characterization of chloro ligands decoordination at the various redox states has now been performed, all constants have been gathered in Table 1. The thermodynamic characteristics of the redox behavior of the system is thus conveniently summarized in Figure 6 in the form of an $E^{0,ap} - \log\left[Cl^-\right]$ diagram with chloride ion concentration conventionally considered as constant (*i.e.* buffered). The Co^{II}/Co^{I} boundary is described by equation (7), whereas the Co^{III}/Co^{II} boundary is given by equation (10):

$$E^{0,ap}_{III/II} = E^{0,2}_{III/II} + \frac{RT}{F}\ln\left(\frac{1+\frac{1}{K_{II,2}\left[Cl^-\right]}+\frac{1}{K_{II,1}K_{II,2}\left[Cl^-\right]^2}}{1+\frac{1}{K_{III,2}\left[Cl^-\right]}+\frac{1}{K_{III,1}K_{III,2}\left[Cl^-\right]^2}}\right) \quad (10)$$

The grey zone in Figure 6 shows the most likely situation, when chloride ions are in solution above mM concentration.

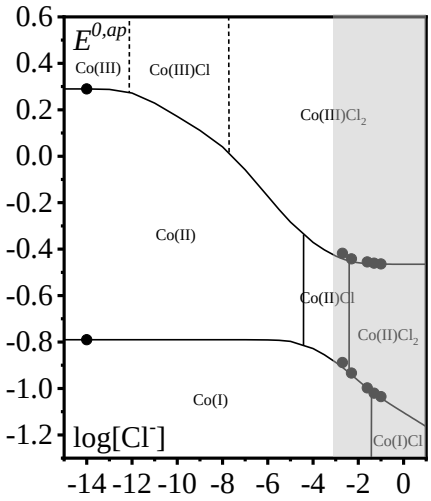

Figure 6. Thermodynamic diagram for the reduction of $[Co^{III}(CR14)Cl_2]^+$ in CH_3CN, 0.1 M $[Bu_4N]ClO_4$ (Cl^- concentration is conventionally considered as constant). $E^{0,ap}$: apparent standard potential vs. Ag^+/Ag. Grey zone: most likely situation, when chloride ions are in solution above mM concentration.

Behavior of $[Co^{III}(CR14)(CH_3CN)_2]^{3+}$ and $[Co^{III}(CR14)Cl_2]^+$) and their reduced Co^{II} forms upon addition of p-cyanoanilinium tetrafluoroborate.

The electrocatalytic behavior of $[Co^{III}(CR14)Cl_2]^+$ in CH_3CN has been investigated in early works by different groups[17, 27, 33, 51,18, 21] in the presence of *p*-cyanoanilinium tetrafluoroborate but also with acid of different strengths such as *p*-toluenesulfonic acid (pK_a = 8.3)[52] and trifluoroacetic acid (pK_a = 12.7).[53] With such relatively strong acids, a catalytic wave develops at potentials very close to the Co^{II}/Co^{I} wave, consistent with hydrogen evolution formed by protonation of the electrochemically generated Co^{I} species.[17-18] In addition, the potential of the Co^{III}/Co^{II} wave is significantly shifted to more positive value and partially loses its reversibility. This latter behavior has been interpreted as resulting from a protonation and decoordination of the amine of the ligand at the Co^{II} state (Scheme 2b).[27] To get more insights into the reactivity/stability of Co^{III} and Co^{II} states in the presence of *p*-cyanoanilinium tetrafluoroborate, UV-Vis spectra of both $[Co^{III}(CR14)]^{3+}$ and $[Co^{II}(CR14)]^{2+}$ have been recorded with increasing amount of added *p*-cyanoanilinium tetrafluoroborate (Figures 7a and 7b). In both cases, no significant change of the UV-Vis spectrum is observed indicating no protonation or decoor-

dination of the complexes. It is in agreement with the invariance of the CV wave of the corresponding $[Co^{III}(CR14)]^{3+}/[Co^{II}(CR14)]^{2+}$ redox couple (Figure 7c). These experiments indicate that there is no protonation and no decoordination of the ligand by *p*-cyanoanilinium tetrafluoroborate, neither at the Co^{III} state nor at the Co^{II} state.

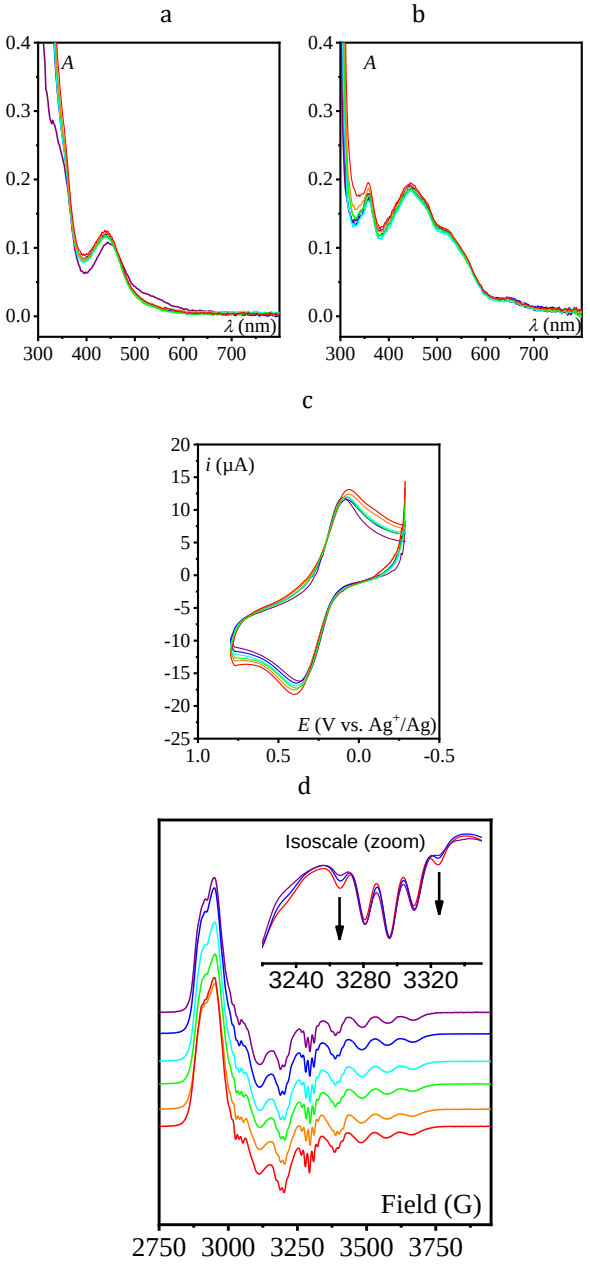

Figure 7. (a) UV-Visible absorption spectra (l = 2 mm) of a 1 mM solution of $[Co^{III}(CR14)(CH_3CN)_2]^{3+}$ in CH_3CN 0.1 M $[Bu_4N]ClO_4$, initial solution (violet) and after addition of increasing amount of *p*-cyanoanilinium tetrafloroborate (AH). (b) UV-Visible absorption spectra (l = 1 mm) of a 1 mM solution of $[Co^{II}(CR14)(CH_3CN)_x]^{2+}$ in CH_3CN 0.1 M $[Bu_4N]ClO_4$, initial solution (violet) and after addition of increasing amount of AH. (c) CV at a 3 mm diameter glassy carbon electrode of a 1 mM solution of $[Co^{III}(CR14)(CH_3CN)_2]^{3+}$ (violet) in CH_3CN, 0.1 M $[Bu_4N]ClO_4$ at 0.1 V/s CV and after addition of increasing amount of AH. (d) X-band EPR spectra at 100 K of electrogenerated solutions in CH_3CN, 0.1 M $[Bu_4N]ClO_4$ of $[Co^{II}(CR14)(CH_3CN)_x]]^{2+}$ 1 mM (violet) and after addition of increasing amount of AH. Insert: zoom of the resonance at 3295 G (isoscale spectra, same color code). Microwave Freq. 9.42 GHz, power 7 mW, Mod. Freq. 100 KHz, Amp. 5 G. In all cases, added concentration of AH: 1 (blue), 2 (light blue), 5 (light green), 10 (orange), 20 (red) mM.

In addition, the EPR spectrum of $[Co^{II}(CR14)(CH_3CN)_x]^{2+}$ (x = 1 or 2) evolves only marginally upon addition of acid (Figure 7d). The most noticeable evolution concerns the ratio of the individual lines in the 5-line superhyperfine structures. The contribution of the outer lines increases with increasing the acid concentration (insert of Figure 7d), consistent with a change in the speciation. These data indicate that the species with two interacting and equivalent ^{14}N nucleus predominates under highly acidic conditions, suggesting the coordination of two nitrogen-based axial ligands, which could be CH_3CN and/or the nitrile of *p*-cyanoanilinium acid (Scheme 1). However, upon addition of a large excess of *p*-cyanoaniline (up to 50 mM) in a 1 mM solution of $[Co^{II}(CR14)(CH_3CN)_x]^{2+}$, no changes are observed on EPR and UV-Vis. spectra (Figures S9 and S10), indicating that the nitrile of *p*-cyanoanilinium does not coordinate to the metal center.

Regarding the chloro complex $[Co^{III}(CR14)Cl_2]^+$ no decoordination of Cl^- occurs for $[Co^{III}(CR14)Cl_2]^+$ upon addition of acid, the resulting UV-Visible spectra being similar to that of the initial one in absence of acid (Figure 8a). By contrast, *p*-cyanoanilinium tetrafluoroborate reacts with $[Co^{II}(CR14)Cl]^+$, the predominant one electron reduced form of $[Co^{III}(CR14)Cl_2]^+$, leading to decoordination of the remaining chloro ligand and formation of $[Co^{II}(CR14)(CH_3CN)_x]^{2+}$ (x = 1 or 2) as attested by UV-Vis (Figure 8b). This decoordination process, corresponding to equation (11), is further unambiguously demonstrated by the evolution of the EPR spectra upon addition of acid. Indeed, the broad spectrum reminiscent of $[Co^{II}(CR14)Cl]^+$ evolves towards the typical spectra of $[Co^{II}(CR14)(CH_3CN)_x]^{2+}$ in presence of 5 equiv. of acid and more (Figures 8c).

$$[Co^{II}(CR14)Cl]^+ + AH \underset{}{\overset{K}{\rightleftharpoons}} [Co^{II}(CR14)]^{2+} + HCl + A^- \quad (11)$$

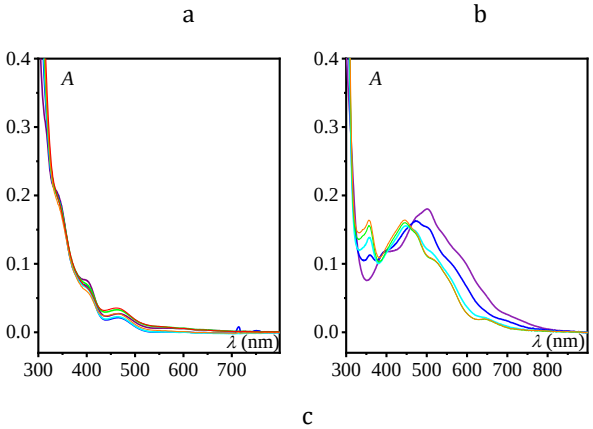

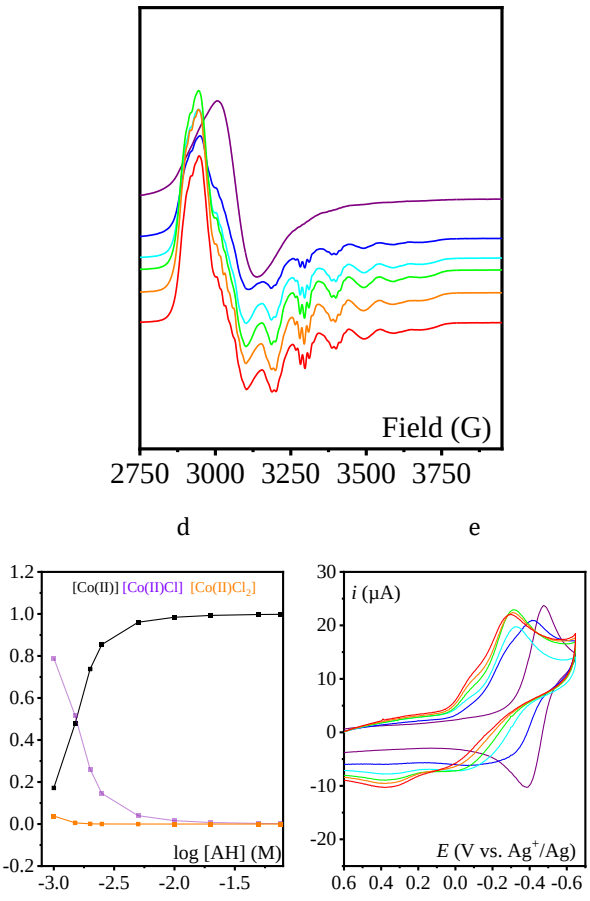

Figure 8. (a) UV-Visible absorption spectra (l = 1 mm) of a 1 mM solution of $[Co^{III}(CR14)Cl_2]^+$ in CH_3CN 0.1 M $[Bu_4N]ClO_4$, initial solution (violet) and after addition of increasing amount of *p*-cyanoanilinium tetrafloroborate (AH). (b) UV-Visible absorption spectra (l = 1 mm) of a 1 mM solution of $[Co^{II}(CR14)Cl]^{2+}$ in CH_3CN 0.1 M $[Bu_4N]ClO_4$, initial solution (violet) and after addition of increasing amount of AH. (c) X-band EPR spectra at 100 K of electrogenerated solutions in CH_3CN, 0.1 M $[Bu_4N]ClO_4$ of $[Co^{II}(CR14)Cl]^+$ 1 mM (violet) and after addition of increasing amount of AH. Microwave Freq. 9.42 GHz, power 7 mW, Mod. Freq. 100 KHz, Amp. 5 G. (d) Speciation of "Co^{II}" species as function of added AH concentration. (e) CV at a 3 mm diameter glassy carbon electrode of a 1 mM solution of $[Co^{III}(CR14)Cl_2]^+$ (violet) in CH_3CN, 0.1 M $[Bu_4N]ClO_4$ at 0.1 V/s CV and after addition of increasing amount of AH. In all cases, added concentration of AH: 1 (blue), 2 (light blue), 5 (light green), 10 (orange), 20 (red) mM.

The equilibrium constant of reaction (11) is $K = \frac{10^{\left[pK_a(\mathrm{HCl}) - pK_a(\mathrm{AH})\right]}}{K_{II,1}}$ where $pK_a(\mathrm{AH}) = 7$ is the pK_a of *p*-cyanoanilinium tetrafluoroborate in acetonitrile and $pK_a(\mathrm{HCl}) = 10.3$ is the pK_a of HCl in acetonitrile. With $K_{II,1} = 3.25\ 10^4\ M^{-1}$, we obtain $K = 0.06$ M from which the speciation of Co^{II} species can be calculated for a solution obtained from one electron reduction of 1 mM of $[Co^{III}(CR14)Cl_2]^+$ in the presence of various amount of *p*-cyanoanilinium tetrafluoroborate. Almost quantitative conversion to $[Co^{II}(CR14)]^{2+}$ is predicted for acid concentrations above 5 mM as observed experimentally showing the consistency of our results (see SI for details). The dynamical aspect of this conversion is observed in Figure 8c showing the CV of the Co^{III}/Co^{II} wave obtained for 1 mM $[Co^{III}(CR14)Cl_2]^+$ in the presence of increasing amount of *p*-cyanoanilinium tetrafluoroborate. A progressive shift to higher potential is observed for the Co^{III} reduction upon addition of acid, a new wave developing at a potential approaching the potential of $[Co^{III}(CR14)]^{3+}/[Co^{II}(CR14)]^{2+}$. Altogether, these results unambiguously demonstrate that the shift towards positive potential of the Co^{III}/Co^{II} wave for the $[Co^{III}(CR14)Cl_2]^+$ complex along with the changes from a broad EPR spectra to a well-resolved spectrum with hyperfine and superhyperfine structure in the presence of acid previously attributed to decoordination and protonation of one amine of the macrocycle ligand[27] are due to the decoordination of one chloro ligand at the Co^{II} oxidation state.

Catalytic behavior.

As recalled in the introduction, $[Co^{III}(CR14)Cl_2]$ has been known for more than a decade to be a catalyst for protons electroreduction in both acetonitrile and aqueous solution. In acetonitrile, with *p*-cyanoanilinium acid as a proton source, a catalytic wave develops at the level of the formal "Co^{II}/Co^{I}" redox couple. Based on the above results and discussion, it clearly appears that, in the presence of an excess of *p*-cyanoanilinium tetrafluoroborate, the species entering the catalytic cycle for hydrogen evolution is $[Co^{II}(CR14)]^{2+}$. Nonetheless, free chloride or HCl molecules can interfere in the mechanism. Therefore, to get intrinsic kinetic information, we have investigated the catalytic HER process starting with $[Co^{II}(CR14)]^{2+}$ in the absence of chloride and with *p*-cyanoanilinium tetrafluoroborate (AH) as a substrate and using cyclic voltammetry as an analytical tool. We note that previous studies have shown that H_2 is produced with > 90% faradaic yield indicating that the catalytic current observed in CV (Figure 9a) can be attributed to acid reduction. Indeed, upon addition of increasing amount of AH to an electrogenerated solution of $[Co^{II}(CR14)]^{2+}$, a catalytic wave develops at the Co^{II}/Co^{I} redox couple level (Figure 9a). Importantly, it is shown that the direct reduction of AH, on the carefully polished glassy carbon electrode, occurs at more negative potential than the first wave observed in the presence of catalyst (see Figure 9b for 100 mM acid concentration and Figure S1 for other acid concentrations). However, at potentials negative to -1V, direct reduction of AH on the glassy carbon electrode interferes, the higher the concentration the more so. Therefore, the mechanistic study is restricted to the -0.6V/-1 V potential range and to acid concentrations below 150 mM.

a b

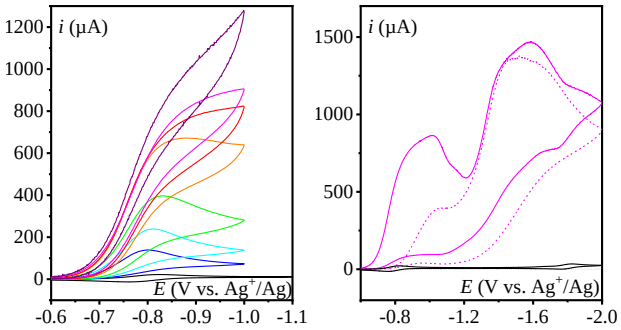

Figure 9. (a) CVs of $[Co^{II}(CR14)]^{2+}$ 1 mM in the absence (black) and in the presence of 5 (blue), 10 (light blue), 20 (green), 50 (orange), 75 (red), 100 (magenta) and 150 (purple) mM of *p*-cyanoanilinium acid; (b) CVs of 100 mM of *p*-cyanoanilinium acid in the absence (dotted line) and in the presence (full line) of 1 mM $[Co^{II}(CR14)]^{2+}$. For (a) and (b): in CH_3CN 0.1 M $[Bu_4N]ClO_4$ at 0.1 V/s on a 3 mm diameter glassy carbon electrode under argon.

Scheme 4. Mechanism for *p*-cyanoanilinium acid electroreduction catalyzed by $[Co^{II}(CR14)]^{2+}$.

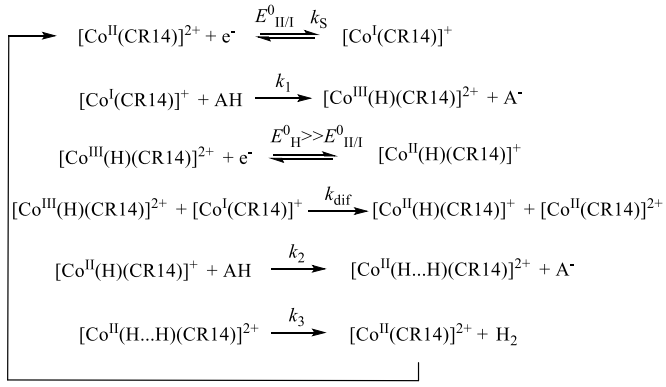

As observed in Figure 9a, the shape of the catalytic wave is evolving from a peak-shape at low acid concentrations to a plateau-shape at high acid concentrations, with, in the latter situation, a current that seems to be only slightly dependent on acid concentration. It is also seen that the onset of the catalytic wave is significantly shifted anodically to the $[Co^{II}(CR14)]^{2+}/[Co^{I}(CR14)]^{+}$ standard potential with a shift that is increasing with the acid concentration. From these observations and building on previous mechanistic studies on *p*-cyanoanilinium reduction catalyzed by cobalt complexes,[27, 54] we propose to analyze the CVs according to the mechanism depicted in Scheme 4 corresponding to an ECE(E')CC mechanism where E denotes an heterogenous electron transfer, E' an homogeneous electron transfer and C a chemical step. All chemical steps are assumed to be irreversible. The standard potential for the reduction of the postulated intermediate hydride $[Co^{III}(H)(CR14)]^{2+}$, E^0_H, is assumed to be more positive than $E^0_{II/I}$, as already indicated in the introduction. Accordingly, the homogenous reduction of $[Co^{III}(H)(CR14)]^{2+}$ by $[Co^{I}(CR14)]^{+}$ is thermodynamically favorable and can be assumed to proceed at diffusion limit with $k_{dif} = 10^{10}$ $M^{-1}s^{-1}$. The competition between heterogeneous and homogeneous reduction of $[Co^{III}(H)(CR14)]^{2+}$ is governed by the parameter $\frac{k_{dif}C^0_{cat}}{k_1 C^0_{AH}}$ which will be shown to be evaluated a posteriori larger than 100 in our experimental conditions (vide infra) leading to the conclusion that $[Co^{III}(H)(CR14)]^{2+}$ is reduced homogeneously and that the mechanism can be simply described with the ECE'CC pathway.

To get quantitative kinetic information out of the catalytic CVs, as a preliminary task, the catalyst redox couple characteristics are determined from CVs recorded in the absence of acid at various scan rates. As shown in Figure S2, the $[Co^{II}(CR14)]^{2+}/[Co^{I}(CR14)]^{+}$ couple has a well-defined nernstian behavior from 0.05 to 1 V/s. with a standard potential $E^0_{II/I}$ = -0.79 V and a peak potential separation of 60 mV. From the peak current $i_p = 0.446FSC^0_{cat}\sqrt{DFv/RT}$, we obtain $D = 1.5\ 10^5$ cm^2/s. Accordingly, a lower limit of the standard rate constant k_S can be evaluated as 0.5 cm/s noting that $\Lambda = k_S\sqrt{\frac{RT}{FvD}}$ has to be larger than 20 for the CV to be nernstian. This lower value of k_S will be used to estimate the possible interference of electron transfer kinetics in the catalytic process. We also observe (Figure S2), that, at a scan rate as low as 0.02 V/s, the CV deviates from the behavior corresponding to semi-infinite one-dimensional diffusion indicating interference from natural convection from which we can evaluate that the maximal diffusion layer size in CV is 150 μm. With this information in hand, we can now analyze the catalytic CVs.

According to the proposed mechanism (ECE'CC), if formation of the hydride $[Co^{III}(H)(CR14)]^{2+}$ is fast enough for pure conditions to be achieved, i.e., $\frac{k_1 C^0_{AH}}{Fv/RT} > 1$, then the foot of the catalytic wave corresponds to:

$$i = \frac{FSC^0_{cat}\sqrt{D}\sqrt{2k_1 C^0_{AH}}}{1+\exp\left[\frac{F}{RT}\left(E - E^0_{II/I}\right)\right]} \qquad (12)$$

Equation (12) is well adjusted to the onset of the catalytic wave at all acids concentrations (from 5 to 150 mM) with $k_1 = 3.3\ 10^5$ $M^{-1}s^{-1}$ (Figure S3). This value allows justifying a posteriori the use of equation (12) because pure kinetics condition ($\frac{k_1 C^0_{AH}}{Fv/RT} >> 1$) is fulfilled and because $[Co^{III}(H)(CR14)]^{2+}$ is reduced homogeneously ($\frac{k_{dif}C^0_{cat}}{k_1 C^0_{AH}} > 100$), hence using the appropriate stoichiometric factor. Our evaluated k_1 value is one order of magnitude larger than the value previously evaluated with $[Co^{III}(CR14)Cl_2]^{+}$ as a catalyst from a foot-of-the-wave analysis and peak potentials in the total catalysis regime.

[27] The discrepancy might result from interference of chloride ions at low acid concentration in previous analysis and/or shift of the peak due to electrode fooling (we observed that careful polishing of the electrode surface is required to get reproducible results). Additionally, if total catalysis regime was not fully reached, then evaluation of the rate constant from the peak potential might be inaccurate.

It is seen in Figure S3, that the actual current in CVs deviates very quickly from equation (12). In the context of the mechanism considered in Scheme 4, there are three factors that may account for such a deviation: (i) kinetic interference of electron transfer kinetics (via k_S), (ii) kinetic interference of chemical steps corresponding to k_2 and/or k_3, (iii) mass transport limitation due to consumption of AH in the diffusion-reaction layer. Other phenomena such as ohmic drop, catalyst degradation or electrode fooling can be source of deviation from the behavior described by equation (12). Careful polishing of the working electrode before each CV rules out electrode fooling. Degradation of the catalyst on the short timescale of the CVs is ruled out from the observation of limited catalyst degradation during long term electrolysis provided the applied potential is not too negative (vide infra). Finally, ohmic drop was partially compensated by the positive feedback system of the potentiostat with a resistance of 150 Ω. Even if the remaining resistance is 50 Ω, its effect at current intensities in the range of 200 µA would only be 10 mV, much smaller than the deviation observed from equation (12) as seen in Figure S3. Therefore, we are left with the listed reasons (i) to (iii). Taking k_S = 0.5 cm/s (vide supra) and using numerical simulations according to the mechanism depicted in Scheme 4 (see SI for details), we take into account the effect of mass transport and evaluate the rate constant k_2. Indeed, for low enough acid concentrations (up to 20 mM), we assume that $k_3 > k_2 C^0_{AH}$ so that the kinetic interference is only due to k_2 (this hypothesis will be validated a posteriori). Hence, a satisfactory simulation of the CVs for C^0_{AH} = 5 to 20 mM is obtained with $k_2 = 2\ 10^4$ $M^{-1}s^{-1}$ (Figure 10a-c). On the contrary, it clearly appears that at higher acid concentrations, the simulated CVs exhibit higher currents than the experimental CVs (Figure S4). We therefore ascribe this effect to the kinetic interference of k_3. Hence, taking the values of k_1 and k_2 determined above, CVs were simulated to evaluate k_3.

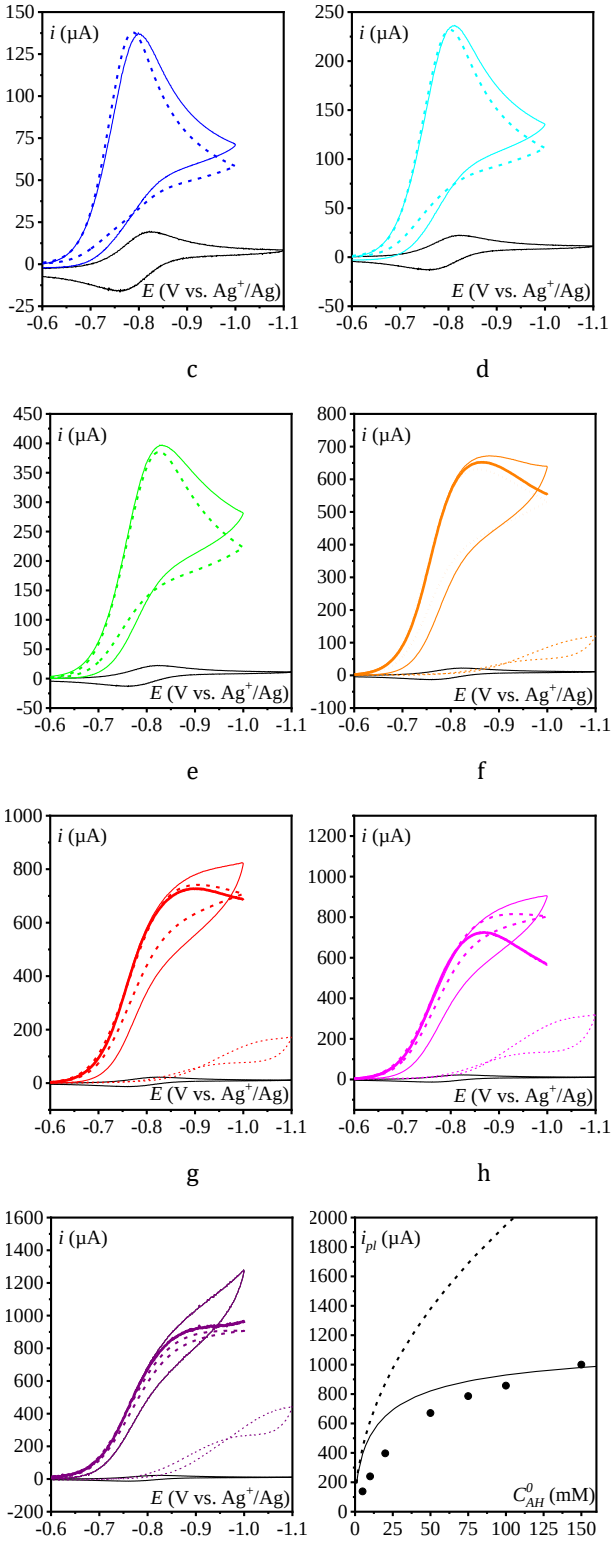

Figure 10. CVs of $[Co^{II}(CR14)]^{2+}$ 1 mM in the absence (black) and in the presence (full thin lines in a to h) of 5 (blue), 10 (light blue), 20 (green), 50 (orange), 75 (red), 100 (magenta) and 150 (purple) mM of *p*-cyanoanilinium acid. From (a) to (h): dashed lines are simulated CVs (see text and SI). From (d) to (g): dotted lines are CVs of the acid alone and thick full lines are forward CV scans obtained after subtraction of the current of the acid alone from the current obtained in the presence of the catalyst.

For (a) and (g): in CH_3CN 0.1 M $[Bu_4N]ClO_4$ at 0.1 V/s on a 3 mm diameter glassy carbon electrode. (h) Dots: peak currents of the CVs as function of the acid concentration; full line: expected plateau current from equation (13); dotted line: expected plateau current from equation (13) if $k_3 \to \infty$.

Because at acid concentrations larger than 50 mM the direct reduction of AH starts to show up in the range of potential of the catalytic wave, this direct reduction was simply considered as being an additive contribution and subtracted. Simulation of the CVs with $k_3 =$ 500 s^{-1} seems to reproduce the current intensities (figure 10d-g) excepted at 100 mM of acid where the direct reduction of acid was maybe overestimated (it is very sensitive to the electrode polishing and not easily reproducible). We thus validate the assumption that $k_3 > k_2 C_{AH}^0$ at the lowest acid concentrations and simulations confirm that k_3 has no significant effect on the CVs at low acid concentrations.

As for k_1 value, the evaluated k_2 value is almost one order of magnitude larger than the previously reported value. The previous value was obtained from plateau currents assuming that this step was the rate determining step at the plateau in the measured conditions. In the framework of the mechanism depicted in Scheme 4, the plateau current that would be reached in absence of mass transport limitation would be given by equation (13):

$$i_{pl} = \frac{FSC_{cat}^0\sqrt{D}}{\left\{\begin{array}{l}\dfrac{1}{\sqrt{2k_1C_{AH}^0}} + \dfrac{1}{\left(\sqrt{2k_1C_{AH}^0}+\sqrt{k_2C_{AH}^0}\right)}\dfrac{\sqrt{k_1}}{\sqrt{2k_2}} \\ + \dfrac{\sqrt{k_2C_{AH}^0}\sqrt{k_1C_{AH}^0}\left[\dfrac{\sqrt{2k_1C_{AH}^0}}{\left(\sqrt{k_2C_{AH}^0}+\sqrt{k_3}\right)}+1\right]}{\left(\sqrt{2k_1C_{AH}^0}+\sqrt{k_2C_{AH}^0}\right)\left(\sqrt{2k_1C_{AH}^0}+\sqrt{k_3}\right)\sqrt{2k_3}}\end{array}\right\}} \qquad (13)$$

Based on this equation, the expected plateau current is represented as function of acid concentrations in figure 10h. It is seen that in our conditions (1 mM catalyst and 0.1 V/s), the plateau current (corresponding to negligible acid consumption in the diffusion-reaction layer) is only reached at the highest concentrations (above 100 mM as observed experimentally). At lower concentrations, mass transport is partially controlling the maximal current in CVs at 0.1 V/s. It is also seen that, if it can be reached (for example by increasing the scan rate), the plateau current is sensitive to k_3, the more so when as the acid concentration increases (comparison of full line and dashed line in Figure 10h). The limit corresponding to a control of the catalysis by k_3 is almost reached at 150 mM acid concentration as this limit would correspond to $i_{pl} = 2FSC_{cat}^0\sqrt{D}\sqrt{k_3} = 1130$ µA. As already discussed elsewhere, the signification of the chemical step with the rate constant k_3 is unclear. It has been proposed to result from a prior protonation of the amine of the cycle thus playing the role of a proton relay with the step corresponding to k_3 being an intramolecular proton transfer from the relay to the hydride to form dihydrogen. However, our experiments show that protonation of the amine of the macrocycle by *p*-cyanoanilinium acid at the Co^{II} state is unlikely (vide supra). It is therefore not obvious to propose such a protonation on the $Co^{II}H$ hydride species. Another suggestion is to consider an irreversible protonation of the hydride with AH (rate constant k_2) leading to a coordinated H_2 (intermediate written as $[Co^{II}(H...H)(CR14)]^{2+}$ in Scheme 4) which is then released with a rate constant k_3.

Despite the uncertainties on the exact nature of the last step of the mechanism leading to release of H_2, the kinetic analysis indicates that the rate determining step of the mechanism is not the first chemical step following the initial electron transfer. Accordingly, the catalytic species that accumulates in the diffusion-reaction layer, i.e., the resting state of the catalyst, is the reduced hydride $[Co^{II}(H)(CR14)]^+$ or the putative H_2 adduct $[Co^{II}(H...H)(CR14)]^{2+}$, depending on the acid concentration. It is exemplified in Figure 11 showing the simulated concentration profiles of the various catalytic species in the diffusion-reaction layer at -1 V during CVs at 0.1 V/s for both 20 mM and 100 mM acid concentrations. At 20 mM acid, the reduced hydride $[Co^{II}(H)(CR14)]^+$ is the dominant catalytic species in the diffusion-reaction layer (along with $[Co^{II}(CR14)]^{2+}$). At 100 mM acid, the diffusion-reaction layer is smaller, in line with faster reactions and both $[Co^{II}(H)(CR14)]^+$ and $[Co^{II}(H...H)(CR14)]^{2+}$ are the dominant catalytic species.

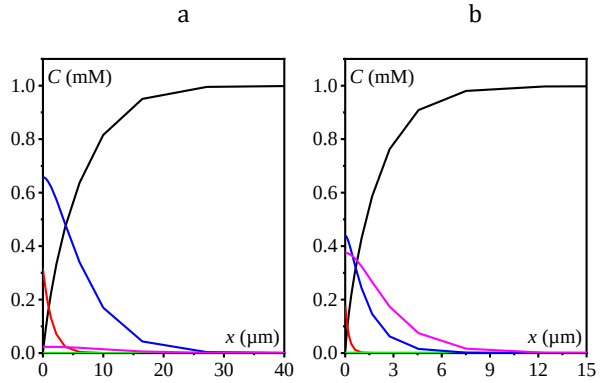

Figure 11. Concentrations profiles at -1 V in simulated CVs at 0.1 V/s with $Co^{II}(CR14)]^{2+}$ 1 mM and AH 20 mM (a) and 100 mM (b) according to the mechanism in Scheme 4 with rate constants given in the text (see SI for details on simulations). Black: $[Co^{II}(CR14)]^{2+}$; red: $[Co^{I}(CR14)]^{+}$; green: $[Co^{III}(H)(CR14)]^{2+}$; blue: $[Co^{II}(H)(CR14)]^{+}$; magenta: $[Co^{II}(H...H)(CR14)]^{2+}$.

The efficiency of $[Co^{II}(CR14)]^{2+}$ as a molecular catalyst for the *p*-cyanoanilinium acid reduction to hydrogen results in the formation of a thin diffusion-reaction layer, thinner than the diffusion layer that is typically set by stirring of the solution in the electrolysis set-up used in our lab. The size of the diffusion layer δ set by the 1000 rpm stirring of the cathodic compartment in our electrolysis set-up can be evaluated as follows. The characteristic time cell corresponding to conversion of a V = 10 mL solution of

$[Co^{III}(CR14)]^{2+}$ into $[Co^{II}(CR14)]^{+}$ on a carbon paper electrode of 2.24 cm^2 at a constant applied potential -0.6 V is $t_c = V\delta / DS = 300$ s (figure S5). Hence, taking D = 1.5 10^{-5} cm^2/s, we obtain $\delta \approx 10\,\mu m$. Accordingly, during an electrolysis at a constant applied potential negative to the standard potential $E^{0,0}_{II/I}$ in the presence of *p*-cyanoanilinium acid, we anticipate the resting state in the bulk to be $[Co^{II}(CR14)]^{2+}$ until consumption of the acid from which $[Co^{II}(CR14)]^{2+}$ should be converted to $[Co^{I}(CR14)]^{+}$. That it is indeed the case shown in Figure 12. A 10 mL solution of 0.9 mM $[Co^{II}(CR14)]^{2+}$ and 20 mM of *p*-cyanoanilinium acid was electrolyzed at a constant applied potential of -0.85 V. A linear increase of the charge passed over time is observed until the passage of 20 C, corresponding to almost complete consumption of acid after 60 min. A control experiment shows that, in the absence of catalyst, the charge passed over the same period of time is only 2 C (Figure 12a) in agreement with the observation of a limited direct reduction of acid at this potential (Figure S1c). The current remains approximately constant during electrolysis at ca. 6 mA until it drops when the acid concentration substantially decreases (Figure S6). Note that the working electrode was a carbon felt which surface area is not well defined.

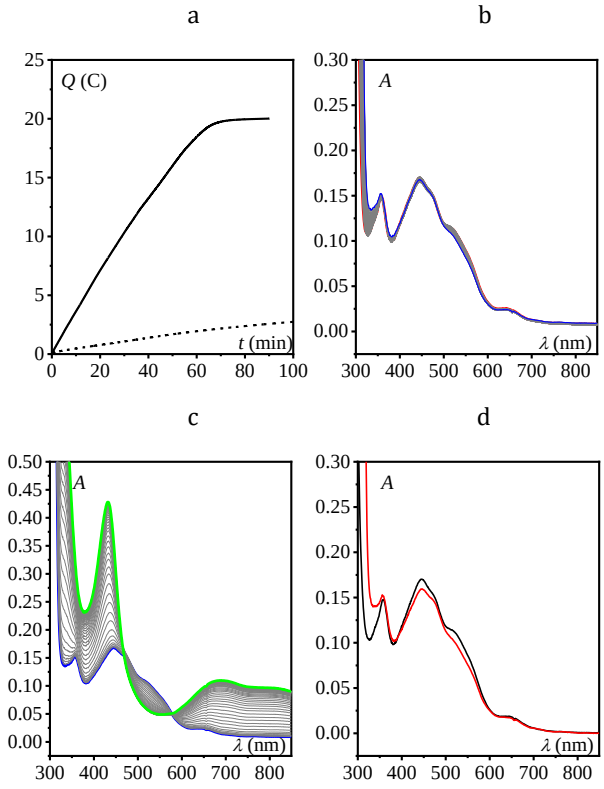

Figure 12. Electrolysis of $[Co^{II}(CR14)]^{2+}$ 0.9 mM + 20 mM *p*-cyanoanilinium acid in CH_3CN 0.1 M $[Bu_4N]ClO_4$ on a carbon felt electrode at -0.85 V. (a) Time evolution of the charge passed (in dashed: charge passed in absence of $[Co^{II}(CR14)]^{2+}$ at the same applied potential). (b) UV-Vis spectra (l = 1 mm) during electrolysis from t = 0 to t = 60 min (one spectrum / 30 s); initial spectrum in red, final spectrum in blue. (c) UV-vis spectra (l = 1 mm) during electrolysis from t = 60 to t = 90 min (one spectrum / 30 s); initial spectrum in blue, final spectrum in green. (d) black: UV-Vis spectrum (l = 1 mm) of $[Co^{II}(CR14)]^{2+}$ before electrolysis; red: UV-Vis spectrum (l = 1 mm) of the electrolytic solution after 90 min electrolysis at -0.85 V followed by electrolysis at -0.4 V.

Monitoring the bulk solution by in situ UV-Vis absorption spectroscopy confirms that (i) catalysis occurs in the diffusion reaction-layer and not in the bulk (fast catalysis), (ii) $[Co^{II}(CR14)]^{2+}$ is the resting state in solution and it is not protonated, (iii) there is no degradation of the catalyst. Figure 12b indeed shows that the in situ recorded UV-Vis spectrum of the bulk solution does not change during the first 60 min of electrolysis. Then after 60 min, when the acid is consumed, $[Co^{II}(CR14)]^{2+}$ starts to be converted to $[Co^{I}(CR14)]^{+}$ (Figure 12c). Electrolysis of the final solution at -0.4 V leads to a conversion of $[Co^{I}(CR14)]^{+}$ back to $[Co^{II}(CR14)]^{2+}$ showing recovery of the initial catalyst (Figure 12d).

The same experiment was carried out at -1.3 V but at this potential, direct reduction of *p*-cyanoanilinium acid at the carbon felt working electrode is substantial (Figure S7a) in line with our observation in cyclic voltammetry on a glassy carbon electrode (Figure S1). Additionally, although the cobalt complex is functioning as a catalyst in the diffusion-reaction layer with a resting state being $[Co^{II}(CR14)]^{2+}$ which is then converted to $[Co^{I}(CR14)]^{+}$ when acid is consumed after about 15 min (Figures S7b and c), we also observe a slow degradation of the catalyst as clearly indicated by the monitoring of the absorbance at 433 nm during electrolysis (Figure S7d) as well as via comparison of the UV-Vis spectrum of the initial solution and of the final solution after electrolysis at -0.4 V to convert $[Co^{I}(CR14)]^{+}$ back to $[Co^{II}(CR14)]^{2+}$ (Figure S7e). This indicates that the applied potential of electrolysis has to be carefully selected to get a stable molecular catalysis.

Conclusion

We reinvestigated the H_2-evolving mechanism catalyzed by the tetra-aza Co(CR14) complex in acetonitrile with *p*-cyanoanilinium acid as a proton source. We have characterized the thermodynamical coordination and decoordination properties of the chloro ligands at the Co^{III}, Co^{II} and Co^{I} formal redox states and we have unambiguously shown that addition of *p*-cyanoanilinium facilitates chloro ligand decoordination at the Co^{II} state rather than protonation of a nitrogen of the ligand. Hence, the pertinent catalyst species to enter the catalytic cycle is $[Co^{II}(CR14)]^{2+}$. Therefore, the mechanism is best analyzed in the absence of chlorides and rate constants, larger than previously estimated, have been obtained. The second proton transfer on the hydride intermediate is slower than formation of the hydride itself making the Co^{II} hydride the resting state in the diffusion-reaction layer. At large acid concentrations, as already reported, a zero order in acid step is rate determining. The exact nature of this step remains unclear. Catalysis is fast and confined in a thin diffusion-reaction layer so that the resting state cannot be easily spectroscopically characterized. Accordingly, the resting state in the solution bulk in the course of constant potential electrolysis is the non-protonated $[Co^{II}(CR14)]^{2+}$ species.

If a too negative potential is applied, direct reduction of the acid interferes to molecular catalysis and the catalyst appears to be less stable.

This study emphasizes that it is crucial to carefully investigate the role of labile ligands (here chlorides) to determine the exact nature of the molecular catalytic species and get a kinetic characterization of small molecules activation in the framework of molecular catalysis of electrochemical reactions with transition metal complexes. In some particular cases, ligand exchanges have detrimental effects in catalysis inducing self-modulation processes as recently shown in the case of N_2O activation.[46, 55]

ASSOCIATED CONTENT

Supporting Information

Experimental details. Additional information on speciation evaluation. Additional CVs. Simulations. Additional data on electrolysis.

ACKNOWLEGMENTS

This work was supported by the Agence Nationale de la Recherche (Labex ARCANE, CBH-EUR-GS, ANR-17-EURE-0003). The NanoBio ICMG (UAR 2607) is acknowledged for providing facilities for NMR and EPR analyses. Dr. Rana Deeba is warmly thanked for performing initial electrolysis experiments.

AUTHOR INFORMATION

Corresponding Authors

marie-noelle.collomb@univ-grenoble-alpes.fr
jerome.fortage@univ-grenoble-alpes.fr
cyrille.costentin@univ-grenoble-alpes.fr

Notes

The authors declare no competing financial interest.

REFERENCES

1. Berardi, S.; Drouet, S.; Francas, L.; Gimbert-Surinach, C.; Guttentag, M.; Richmond, C.; Stoll, T.; Llobet, A., Molecular Artificial Photosynthesis. *Chem. Soc. Rev.* **2014,** *43* (22), 7501-7519.
2. Dalle, K. E.; Warnan, J.; Leung, J. J.; Reuillard, B.; Karmel, I. S.; Reisner, E., Electro- and Solar-Driven Fuel Synthesis with First Row Transition Metal Complexes. *Chem. Rev.* **2019,** *119* (4), 2752-2875.
3. Lim, R. J.; Xie, M.; Sk, M. A.; Lee, J.-M.; Fisher, A.; Wang, X.; Lim, K. H., A review on the electrochemical reduction of CO2 in fuel cells, metal electrodes and molecular catalysts. *Catal. Today* **2014,** *233*, 169-180.
4. Qiao, J.; Liu, Y.; Hong, F.; Zhang, J., A review of catalysts for the electroreduction of carbon dioxide to produce low-carbon fuels. *Chem. Soc. Rev.* **2014,** *43* (2), 631-675.
5. Eckenhoff, W. T.; Eisenberg, R., Molecular systems for light driven hydrogen production. *Dalton Trans.* **2012,** *41* (42), 13004-13021.
6. Simmons, T. R.; Berggren, G.; Bacchi, M.; Fontecave, M.; Artero, V., Mimicking hydrogenases: From biomimetics to artificial enzymes. *Coord. Chem. Rev.* **2014,** *270*, 127-150.
7. Artero, V.; Chavarot-Kerlidou, M.; Fontecave, M., Splitting Water with Cobalt. *Angew. Chem. Int. Ed.* **2011,** *50*, 7238-7266.
8. Gao, S.; Fan, W.; Liu, Y.; Jiang, D.; Duan, Q., Artificial water-soluble systems inspired by [FeFe]-hydrogenases for electro- and photocatalytic hydrogen production. *Int. J. Hydrogen Energy* **2020,** *45* (7), 4305-4327.
9. Queyriaux, N.; Jane, R. T.; Massin, J.; Artero, V.; Chavarot-Kerlidou, M., Recent developments in hydrogen evolving molecular cobalt(II)–polypyridyl catalysts. *Coord. Chem. Rev.* **2015,** *304*, 3-19.
10. Eckenhoff, W. T., Molecular catalysts of Co, Ni, Fe, and Mo for hydrogen generation in artificial photosynthetic systems. *Coord. Chem. Rev.* **2018,** *373*, 295-316.
11. Tong, L.; Duan, L.; Zhou, A.; Thummel, R. P., First-row transition metal polypyridine complexes that catalyze proton to hydrogen reduction. *Coord. Chem. Rev.* **2020,** *402*, 213079.
12. Droghetti, F.; Amati, A.; Ruggi, A.; Natali, M., Bioinspired motifs in proton and CO2 reduction with 3d-metal polypyridine complexes. *Chem. Commun.* **2024,** *60* (6), 658-673.
13. Bourrez, M.; Molton, F.; Chardon-Noblat, S.; Deronzier, A., Mn(bipyridyl)(CO)(3)Br : An Abundant Metal Carbonyl Complex as Efficient Electrocatalyst for CO2 Reduction. *Angew. Chem., Int. Ed. Engl.* **2011,** *50* (42), 9903-9906.
14. Fernandez, S.; Dubed Bandomo, G. C.; Lloret-Fillol, J., Manganese Complexes for Electro- and Photocatalytic Transformations. In *Manganese Catalysis in Organic Synthesis*, 2021; pp 137-181.
15. Long, K. M.; Busch, D. H., Cobalt(II) complexes of the quadridentate macrocycle 2,12-dimethyl-3,7,11,17-tetraazabicyclo[11.3.1]heptadeca-1(17),2,11,13,15-pentaene. *Inorg. Chem.* **1970,** *9* (3), 505-512.
16. McCrory, C. C. L.; Uyeda, C.; Peters, J. C., Electrocatalytic Hydrogen Evolution in Acidic Water with Molecular Cobalt Tetraazamacrocycles. *J. Am. Chem. Soc.* **2012,** *134* (6), 3164-3170.
17. Leung, C. F.; Chen, Y. Z.; Yu, H. Q.; Yiu, S. M.; Ko, C. C.; Lau, T. C., Electro- and photocatalytic hydrogen generation in acetonitrile and aqueous solutions by a cobalt macrocyclic Schiff-base complex. *Int. J. Hydrogen Energy* **2011,** *36* (18), 11640-11645.
18. Varma, S.; Castillo, C. E.; Stoll, T.; Fortage, J.; Blackman, A. G.; Molton, F.; Deronzier, A.; Collomb, M.-N., Efficient Photocatalytic Hydrogen Production in Water Using a Cobalt(III) Tetraaza-Macrocyclic Catalyst: Electrochemical Generation of the Low-Valent Co(I) Species and its Reactivity Toward Proton Reduction. *Phys. Chem. Chem. Phys.* **2013,** *15* (40), 17544-17552.
19. Gueret, R.; Castillo, C. E.; Rebarz, M.; Thomas, F.; Hargrove, A.-A.; Pécaut, J.; Sliwa, M.; Fortage, J.; Collomb, M.-N., Cobalt(III) Tetraaza-Macrocyclic Complexes as Efficient Catalyst for Photoinduced Hydrogen Production in Water: Theoretical Investigation of the Electronic Structure of the Reduced Species and Mechanistic Insight. *J. Photochem. Photobiol., B* **2015,** *152*, 82-94.
20. Gueret, R.; Poulard, L.; Oshinowo, M.; Chauvin, J.; Dahmane, M.; Dupeyre, G.; Lainé, P. P.; Fortage, J.; Collomb, M.-N., Challenging the $[Ru(bpy)_3]^{2+}$ Photosensitizer with a Triazatriangulenium Robust Organic Dye for Visible-Light-Driven Hydrogen Production in Water. *ACS Catal.* **2018,** *8* (5), 3792-3802.
21. Gueret, R.; Castillo, C. E.; Rebarz, M.; Thomas, F.; Sliwa, M.; Chauvin, J.; Dautreppe, B.; Pécaut, J.; Fortage, J.; Collomb, M.-N., Cobalt(II) Pentaaza-Macrocyclic Schiff Base Complex as Catalyst for Light-Driven Hydrogen Evolution in Water: Electrochemical Generation and Theoretical Investigation of the One-Electron Reduced Species. *Inorg. Chem.* **2019,** *58* (14), 9043-9056.
22. Wang, J.-W.; Yamauchi, K.; Huang, H.-H.; Sun, J.-K.; Luo, Z.-M.; Zhong, D.-C.; Lu, T.-B.; Sakai, K., A Molecular Cobalt Hydrogen Evolution Catalyst Showing High Activity and Outstanding Tolerance to CO and O2. *Angew. Chem. Int. Ed.* **2019,** *58* (32), 10923-10927.
23. Gimbert-Surinach, C.; Albero, J.; Stoll, T.; Fortage, J.; Collomb, M.-N.; Deronzier, A.; Palomares, E.; Llobet, A., Efficient and Limiting Reactions in Aqueous Light-Induced Hydrogen Evolution Systems using Molecular Catalysts and Quantum Dots. *J. Am. Chem. Soc.* **2014,** *136* (21), 7655-7661.
24. Roy, S.; Bacchi, M.; Berggren, G.; Artero, V., A Systematic Comparative Study of Hydrogen-Evolving Molecular Catalysts in Aqueous Solutions. *Chemsuschem* **2015,** *8* (21), 3632-3638.
25. Moonshiram, D.; Gimbert-Suriñach, C.; Guda, A.; Picon, A.; Lehmann, C. S.; Zhang, X.; Doumy, G.; March, A. M.; Benet-Buchholz, J.; Soldatov, A.; Llobet, A.; Southworth, S. H., Tracking the Structural and Electronic Configurations of a Cobalt Proton Reduction Catalyst in Water. *J. Am. Chem. Soc.* **2016,** *138* (33), 10586-10596.
26. Sandroni, M.; Gueret, R.; Wegner, K. D.; Reiss, P.; Fortage, J.; Aldakov, D.; Collomb, M. N., Cadmium-free $CuInS_2$/ZnS quantum dots as efficient and robust photosensitizers in combination with a molecular catalyst for visible light-driven H_2 production in water. *Energy Environ. Sci.* **2018,** *11* (7), 1752-1761.
27. Li, C.-B.; Bagnall, A. J.; Sun, D.; Rendon, J.; Koepf, M.; Gambarelli, S.; Mouesca, J.-M.; Chavarot-Kerlidou, M.; Artero, V., Electrocatalytic reduction of protons to dihydrogen by the cobalt tetraazamacrocyclic complex [Co(N4H)Cl2]+: mechanism and benchmarking of performances. *Sustainable Energy & Fuels* **2022,** *6* (1), 143-149.
28. Bold, S.; Straistari, T.; Muñoz-García, A. B.; Pavone, M.; Artero, V.; Chavarot-Kerlidou, M.; Dietzek, B., Investigating Light-Induced Processes in Covalent Dye-Catalyst Assemblies for Hydrogen Production. *Catalysts* **2020,** *10* (11), 1340.
29. Bold, S.; Massin, J.; Giannoudis, E.; Koepf, M.; Artero, V.; Dietzek, B.; Chavarot-Kerlidou, M., Spectroscopic Investigations Provide a Rationale for the Hydrogen-Evolving

Activity of Dye-Sensitized Photocathodes Based on a Cobalt Tetraazamacrocyclic Catalyst. *ACS Catal.* **2021,** *11* (6), 3662-3678.
30. Grau, S.; Schilling, M.; Moonshiram, D.; Benet-Buchholz, J.; Luber, S.; Llobet, A.; Gimbert-Suriñach, C., Electrochemically and Photochemically Induced Hydrogen Evolution Catalysis with Cobalt Tetraazamacrocycles Occurs Through Different Pathways. *ChemSusChem* **2020,** *13* (10), 2745-2752.
31. Camara, F.; Aguirre-Araque, J. S.; Fortage, J.; Collomb, M.-N., Enhancing the stability of photocatalytic systems for hydrogen evolution in water by using a tris-phenyl-phenanthroline sulfonate ruthenium photosensitizer. *Sustainable Energy & Fuels* **2024,** *8* (7), 1457-1472.
32. Tinnemans, A. H. A.; Koster, T. P. M.; Thewissen, D. H. M. W.; Mackor, A., TETRAAZA-MACROCYCLIC COBALT(II) AND NICKEL(II) COMPLEXES AS ELECTRON-TRANSFER AGENTS IN THE PHOTO(ELECTRO)CHEMICAL AND ELECTROCHEMICAL REDUCTION OF CARBON-DIOXIDE. *Recl. Trav. Chim. Pays-Bas* **1984,** *103* (10), 288-295.
33. Lacy, D. C.; McCrory, C. C. L.; Peters, J. C., Studies of Cobalt-Mediated Electrocatalytic CO_2 Reduction Using a Redox-Active Ligand. *Inorg. Chem.* **2014,** *53* (10), 4980-4988.
34. Zhang, M.; El-Roz, M.; Frei, H.; Mendoza-Cortes, J. L.; Head-Gordon, M.; Lacy, D. C.; Peters, J. C., Visible Light Sensitized CO_2 Activation by the Tetraaza $[Co^{II}N_4H(MeCN)]^{2+}$ Complex Investigated by FT-IR Spectroscopy and DFT Calculations. *J. Phys. Chem. C* **2015,** *119* (9), 4645-4654.
35. Sheng, H.; Frei, H., Direct Observation by Rapid-Scan FT-IR Spectroscopy of Two-Electron-Reduced Intermediate of Tetraaza Catalyst [CoIIN4H(MeCN)]2+ Converting CO2 to CO. *J. Am. Chem. Soc.* **2016,** *138* (31), 9959-9967.
36. Nie, W.; Tarnopol, D. E.; McCrory, C. C. L., Enhancing a Molecular Electrocatalyst's Activity for CO2 Reduction by Simultaneously Modulating Three Substituent Effects. *J. Am. Chem. Soc.* **2021,** *143* (10), 3764-3778.
37. Boutin, E.; Merakeb, L.; Ma, B.; Boudy, B.; Wang, M.; Bonin, J.; Anxolabéhère-Mallart, E.; Robert, M., Molecular catalysis of CO2 reduction: recent advances and perspectives in electrochemical and light-driven processes with selected Fe, Ni and Co aza macrocyclic and polypyridine complexes. *Chem. Soc. Rev.* **2020,** *49* (16), 5772-5809.
38. Chen, L.; Guo, Z.; Wei, X.-G.; Gallenkamp, C.; Bonin, J.; Anxolabehere-Mallart, E.; Lau, K.-C.; Lau, T.-C.; Robert, M., Molecular Catalysis of the Electrochemical and Photochemical Reduction of CO_2 with Earth-Abundant Metal Complexes. Selective Production of CO vs HCOOH by Switching of the Metal Center. *J. Am. Chem. Soc.* **2015,** *137* (34), 10918-10921.
39. Wang, J.-W.; Huang, H.-H.; Wang, P.; Yang, G.; Kupfer, S.; Huang, Y.; Li, Z.; Ke, Z.; Ouyang, G., Co-facial π−π Interaction Expedites Sensitizer-to-Catalyst Electron Transfer for High-Performance CO2 Photoreduction. *JACS Au* **2022,** *2* (6), 1359-1374.
40. Wang, J.-W.; Gil-Sepulcre, M.; Huang, H.-H.; Solano, E.; Mu, Y.-F.; Llobet, A.; Ouyang, G., CH-π interaction boosts photocatalytic CO2 reduction activity of a molecular cobalt catalyst anchored on carbon nitride. *Cell Reports Physical Science* **2021,** *2* (12), 100681.
41. Bagnall, A. J.; Haake, M.; Grau, S.; Straistari, T.; Koepf, M.; Jameei Moghaddam, N.; Gimbert-Suriñach, C.; Benet-Buchholz, J.; Llobet, A.; Chavarot-Kerlidou, M.; Reuillard, B.; Artero, V., Molecular Engineering of Electrocatalytic Nanomaterials for Hydrogen Evolution: The Impact of Structural and Electronic Modifications of Anchoring Linkers on Electrocatalysis. *ACS Catal.* **2024,** *14* (8), 5630-5638.
42. Bagnall, A. J.; Eliasson, N.; Hansson, S.; Chavarot-Kerlidou, M.; Artero, V.; Tian, H.; Hammarström, L., Ultrafast Electron Transfer from CuInS2 Quantum Dots to a Molecular Catalyst for Hydrogen Production: Challenging Diffusion Limitations. *ACS Catal.* **2024,** *14* (6), 4186-4201.
43. Andrin, B.; Marques Cordeiro Junior, P. J.; Provost, D.; Diring, S.; Pellegrin, Y.; Robert, M.; Odobel, F., Carbon nanotube heterogenization improves cobalt pyridyldiimine complex CO2 reduction activity in aqueous carbonate buffer. *Chem. Commun.* **2024,** *60* (38), 5022-5025.
44. Costentin, C.; Camara, F.; Fortage, J.; Collomb, M.-N., Photoinduced Catalysis of Redox Reactions. Turnover Numbers, Turnover Frequency, and Limiting Processes: Kinetic Analysis and Application to Light-Driven Hydrogen Production. *ACS Catal.* **2022**, 6246-6254.
45. Fortage, J.; Collomb, M.-N.; Costentin, C., Turnover Number in Photoinduced Molecular Catalysis of Hydrogen Evolution: a Benchmarking for Catalysts? *ChemSusChem* **2024,** *n/a* (n/a), e202400205.
46. Chartier, C.; Chardon-Noblat, S.; Costentin, C., Redox Behavior and Kinetics of Hydroxo Ligand Exchange on Iron Tetraphenylporphyrin: Comparison with Chloro Exchange and Consequences for Its Role in Self-Modulation of Molecular Catalysis of Electrochemical Reactions. *Inorg. Chem.* **2024,** *63* (17), 7541-7548.
47. Blackman, A. G., Cobalt: Inorganic and Coordination Chemistry. *Encyclopedia of Inorganic Chemistry, 2nd ed., (Ed.: R. B. King), Wiley* **2006**, p. 967-991.
48. Pezeshk, A.; Greenaway, F. T.; Dabrowiak, J. C.; Vincow, G., EPR STUDIES OF AXIAL LIGATION OF A LOW-SPIN COBALT(II) MACROCYCLIC SCHIFF-BASE COMPLEX. *Inorg. Chem.* **1978,** *17* (7), 1717-1725.
49. Magri, G.; Folli, A.; Murphy, D. M., Monitoring the Substrate-Induced Spin-State Distribution in a Cobalt(II)-Salen Complex by EPR and DFT. *Eur. J. Inorg. Chem.* **2022,** *2022* (9), e202101071.
50. Cropek, D. M.; Metz, A.; Muller, A. M.; Gray, H. B.; Horne, T.; Horton, D. C.; Poluektov, O.; Tiede, D. M.; Weber, R. T.; Jarrett, W. L.; Phillips, J. D.; Holder, A. A., A novel ruthenium(II)-cobaloxime supramolecular complex for photocatalytic H-2 evolution: synthesis, characterisation and mechanistic studies. *Dalton Trans.* **2012,** *41* (42), 13060-13073.
51. Lee, C. H.; Villágran, D.; Cook, T. R.; Peters, J. C.; Nocera, D. G., Pacman and Hangman Metal Tetraazamacrocycles. *ChemSusChem* **2013,** *6* (8), 1541-1544.
52. Fourmond, V.; Jacques, P. A.; Fontecave, M.; Artero, V., H_2 Evolution and Molecular Electrocatalysts: Determination of Overpotentials and Effect of Homoconjugation. *Inorg. Chem.* **2010,** *49* (22), 10338-10347.
53. Raamat, E.; Kaupmees, K.; Ovsjannikov, G.; Trummal, A.; Kütt, A.; Saame, J.; Koppel, I.; Kaljurand, I.; Lipping, L.; Rodima, T.; Pihl, V.; Koppel, I. A.; Leito, I., Acidities of strong neutral Brønsted acids in different media. *J. Phys. Org. Chem.* **2013,** *26* (2), 162-170.
54. Rountree, E. S.; Martin, D. J.; McCarthy, B. D.; Dempsey, J. L., Linear Free Energy Relationships in the Hydrogen Evolution Reaction: Kinetic Analysis of a Cobaloxime Catalyst. *ACS Catal.* **2016,** *6* (5), 3326-3335.
55. Deeba, R.; Chardon-Noblat, S.; Costentin, C., Importance of Ligand Exchange in the Modulation of Molecular Catalysis: Mechanism of the Electrochemical Reduction of Nitrous Oxide with Rhenium Bipyridyl Carbonyl Complexes. *ACS Catal.* **2023,** *13* (12), 8262-8272.